Journal of Ocean Engineering and Marine Energy (2024) 10:275–286
https://doi.org/10.1007/s40722-023-00312-y

RESEARCH

A practical wave flume layout to test reflective models without any need for an active absorption system

Saeed Mahjouri[1] · Saeed Pashazanousi[1] · Rasoul Shabani[1] · Saeed Tariverdilo[2]

Received: 21 September 2023 / Accepted: 15 December 2023 / Published online: 2 February 2024

Abstract
Introducing a new flume layout with bottom-mounted wavemaker in the presence of fully reflective model, this paper investigates how it could be effectively utilized to eliminate different source of wave reflections. Compared with common type wave makers, bottom-mounted wavemakers could effectively eliminate wave re-reflections from the wavemaker. This paper uses analytical solution based on velocity potential to derive wave propagation for steady state excitation, where the results is verified by ANSYS CFX. It is shown that using the proposed layout it is possible, (a) to diminish the disturbing effect of re-reflection of progressive waves from the wavemaker and also to remove the possibility of resonance, and (b) to decrease the distance from the wavemaker to the absorbing beach, which results in the shorter flume length. These finding show that using the proposed layout, there is no need to use active absorbing wavemaker.

Keywords Velocity potential theory · Reflective model · Bottom-mounted wavemaker · Active absorption · Flume layout

List of symbols

b	Paddle length (m)
g	Gravity acceleration (m s^{-2})
h	Still water height (m)
η	Wave height (m)
H	Wave amplitude (m)
L	Location of the test model (m)
k_p	Wave number of progressive wave
k_{sn}	Wave number of evanescent waves
$\overline{k}_{sn}$	Wave number of additional evanescent waves
S	Paddle amplitude (m)
ω	Paddle angular frequency (s^{-1})
$\varphi_1, \varphi_2, \varphi_3, \varphi_4$	Velocity potential functions

✉ Rasoul Shabani
r.shabani@urmia.ac.ir

Saeed Mahjouri
saeed.mahjouri.sm@gmail.com

Saeed Pashazanousi
st_s.pashazanousi@urmia.ac.ir

Saeed Tariverdilo
s.tariverdilo@urmia.ac.ir

[1] Department of Mechanical Engineering, Faculty of Engineering, Urmia University, Urmia, Iran

[2] Department of Civil Engineering, Faculty of Engineering, Urmia University, Urmia, Iran

1 Introduction

In the flumes dissipating beach is used to absorb incoming waves and prevent their reflections. However, these absorbers do not have any impact on the waves reflecting from the test models back to the wavemaker. This interaction between the model and the wave paddle could lead to multiple reflections of the waves. These reflections have the potential to alter the frequency composition of the intended incident wave or even induce resonance (Mahjouri et al. 2020a, b).

To avoid exposure to re-reflected waves, different passive methods have been employed by different researchers. One of the traditional ways is to use long wave flumes and stop the test before the reflected waves reach the wave paddle (Machado et al. 2018). Another common method is to use the test models whose width is significantly smaller than the width of the flume; however, this method is not able to fully eliminate the incident waves.

An effective approach to prevent re-reflections or absorb the reflected waves is to use absorbing wavemakers, where

a hydrodynamic feedback and an absorption control algorithm are utilized to generate the prescribed incident waves and simultaneously absorb the unwanted re-reflected waves. Different design and implementation of the absorbing wavemakers could be found in the literature. Milgram (1970) employed a wave elevation gauge as a means of hydraulic feedback and incorporated an absorption mechanism within a flap-type wavemaker. In a similar context, Hirakuchi and his colleagues (1990) devised a piston-type absorbing wavemaker, incorporating a wave gauge to serve as hydraulic feedback. Christensen and Frigaard (1994) utilized a pair of wave gauges to serve as hydrodynamic feedbacks in order to devise an innovative active absorption system. Schäffer and Jakobsen (2003) have proposed IIR digital filter to approximate the absorption transfer function. In 2016, Yang and colleagues introduced a novel approach for estimating the absorption transfer function by utilizing an iterative reweighted least-squares procedure. Yang et al. (2015) have developed a remarkable absorption system for a piston-type wave generator. Recently, Mahjouri et al. (2020a, b) introduced a simple and practical absorbing algorithm in the time domain and implemented it in a piston-type wavemaker. It is important to acknowledge that for absorbing wavemakers to function effectively, precise measuring equipment, electronic interfaces, and controller design are essential (Schäffer and Klopman 2000). Furthermore, the shape of the paddle, potential noise, and uncertainties in the model may impact the performance of the absorbing wavemaker (Maguire and Ingram 2011).

Recently, Mahjouri et al. (2020a, b) proposing a bottom-mounted wavemaker investigated its performance in a flume with infinite length without reflective model. Accounting for the presence of reflective test model in the fluid domain, this paper proposes a unique and practical layout to test the reflective models without any need for an absorbing wavemaker. The proposed layout includes a bottom-mounted hinge-type wavemaker, a test model located on one side of the wavemaker, and a radiation boundary condition on the opposite side. Oscillation of the bottom paddles produces an upward flow and, subsequently, progressive surface waves, which propagates toward the test model and also radiation boundary.

This paper investigates how bottom-mounted wavemaker could be employed to suppress different source of wave reflection, i.e., wave reflection from absorbing beach, test model and the wavemaker itself. To do this, first the analytical solution for the proposed layout is developed employing velocity potential. Then the results of analytical solution are verified employing ANSYS CFX. Finally, efficiency of the proposed layout in suppressing different types of wave reflections is investigated.

2 Mathematical modeling

Figure 1 shows the proposed flume layout, where the reflective test model is located on the right side of the wavemaker, and an absorbing beach is considered on the opposite side. A symmetrical hinge-type wavemaker is considered at the bottom to produce upward flow and, consequently the surface waves. Considering the small vibration amplitude of the paddles ($S = 0.1\ h$), the gap or discontinuity at the endpoints of the paddles has no significant impact and is not included in the mathematical modeling. Nevertheless, in the practical applications to prevent local turbulent flows, the endpoints can be connected or covered by an elastic membrane. The y-coordinate represents the vertical direction, with its starting point at the bottom of the channel. On the other hand, the x-coordinate represents the horizontal direction, with its starting point at the right edge of the paddle. We assume that the channel is filled to a height of h, and the paddles vibrate harmonically, with their average position corresponding to $y = 0$. This analytical solution is in frequency domain and only considers steady state excitation.

Assuming inviscid and incompressible fluid flow, the fluid field is divided into four regions, and four different velocity functions is employed to model the fluid field. This velocity potential functions should satisfy the following Laplace equations (Zhou et al. (2010))

$$\nabla^2\varphi_1 = 0, \quad 0 \le y \le h, \quad -b \le x \le 0, \tag{1}$$

$$\nabla^2\varphi_2 = 0, \quad 0 \le y \le h, \quad 0 \le x \le L, \tag{2}$$

$$\nabla^2\varphi_3 = 0, \quad 0 \le y \le h, \quad -2b \le x \le -b, \tag{3}$$

$$\nabla^2\varphi_4 = 0, \quad 0 \le y \le h, \quad -\infty \le x \le -2b. \tag{4}$$

It is assumed that the motion of the paddles is harmonic and in phase in the first and third fluid regions. They vibrate with functions $S_1(x)\sin(k_p b + \omega t)$ and $S_2(x)\sin(k_p b + \omega t)$, where ω is the forcing frequency, k_p is the wave number, and b is the paddle length. $S_1(x)$ and $S_2(x)$ represent the geometry of the wave paddles, which can be any arbitrary functions, and in the proposed hinge-type paddles, they are straight-line functions. The only requirements for these functions are that they should become zero at $x = 0$ and $-2b$, and equal to each other at $x = -b$.The velocity potential function in the region 1 should satisfy the following boundary conditions

$$g\frac{\partial\varphi_1}{\partial y} + \frac{\partial^2\varphi_1}{\partial t^2}\bigg|_{y=h} = 0, \tag{5}$$

$$\frac{\partial\varphi_1}{\partial y}\bigg|_{y=0} = \omega S_1(x)\cos(k_p b + \omega t), \tag{6}$$

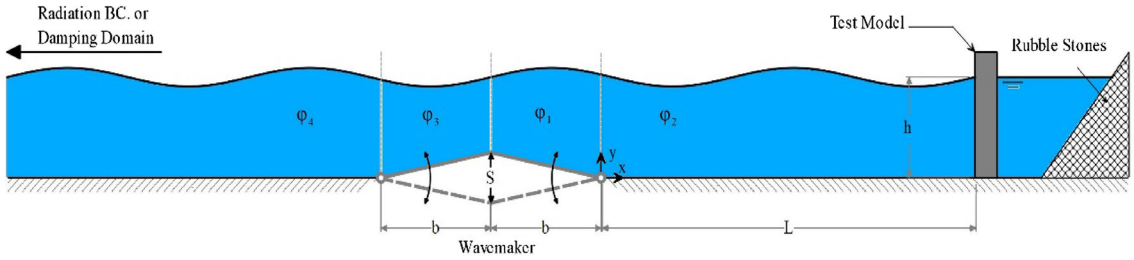

Fig. 1 Schematic layout considered in the analytical derivation

where g denotes the acceleration of gravity. Equation (5) is the free surface condition, and Eq. (6) describes the linear kinematic boundary condition on the wave paddle (Dean and Dalrymple 1991).

The boundary conditions for fluid flow in region φ_2 are

$$\left.\frac{\partial \varphi_2}{\partial x}\right|_{x=L} = 0, \tag{7}$$

$$\left.\frac{\partial \varphi_2}{\partial y}\right|_{y=0} = 0, \tag{8}$$

$$\left.g\frac{\partial \varphi_2}{\partial y} + \frac{\partial^2 \varphi_2}{\partial t^2}\right|_{y=h} = 0. \tag{9}$$

Equations (7) and (8) describe the no-flow conditions on the test model and bottom of this region, respectively, and the free surface condition is covered by Eq. (9).

For the third region, the free surface condition and the linear kinematic boundary condition on the associated wave paddle are stated as

$$\left.g\frac{\partial \varphi_3}{\partial y} + \frac{\partial^2 \varphi_3}{\partial t^2}\right|_{y=h} = 0, \tag{10}$$

$$\left.\frac{\partial \varphi_3}{\partial y}\right|_{y=0} = \omega S_2(x)\cos(k_p b + \omega t). \tag{11}$$

In the same way, the boundary condition for the fourth fluid region will be

$$\left.g\frac{\partial \varphi_4}{\partial y} + \frac{\partial^2 \varphi_4}{\partial t^2}\right|_{y=h} = 0, \tag{12}$$

$$\left.\frac{\partial \varphi_4}{\partial y}\right|_{y=0} = 0, \tag{13}$$

radiation condition at $x \to -\infty$.

In addition, the kinematic matching conditions must be satisfied at the common boundaries of the regions, which means

$$\left.\frac{\partial \varphi_1}{\partial x} = \frac{\partial \varphi_2}{\partial x}\right|_{x=0}, \quad \left.\frac{\partial \varphi_1}{\partial y} = \frac{\partial \varphi_2}{\partial y}\right|_{x=0}, \tag{14}$$

$$\left.\frac{\partial \varphi_1}{\partial x} = \frac{\partial \varphi_3}{\partial x}\right|_{x=-b}, \quad \left.\frac{\partial \varphi_1}{\partial y} = \frac{\partial \varphi_3}{\partial y}\right|_{x=-b}, \tag{15}$$

$$\left.\frac{\partial \varphi_3}{\partial x} = \frac{\partial \varphi_4}{\partial x}\right|_{x=-2b}, \quad \left.\frac{\partial \varphi_3}{\partial y} = \frac{\partial \varphi_4}{\partial y}\right|_{x=-2b}. \tag{16}$$

The general solution for the velocity potential function φ_1 becomes

$$\varphi_1 = A\cos h(k_p y)[\sin(k_p x - \omega t) + \sin(2k_p L - k_p x - \omega t)] + \cos(k_p b + \omega t)\left[\begin{array}{l}(B+cx)\left(\overline{h}-h+y\right) + e^{\frac{y}{\overline{h}}}\left(\overline{A}\cos\left(\frac{x}{\overline{h}}\right) + \overline{B}\sin\left(\frac{x}{\overline{h}}\right)\right) \\ +\sum_{n=1}^{N}\left(\overline{D}_{1n}e^{-\overline{k}_{sn}x} + \overline{D}'_{1n}e^{\overline{k}_{sn}x}\right)\sin\left(\overline{k}_{sn}y\right) \\ +\sum_{n=1}^{N}\left(D_{1n}e^{-k_{sn}x} + D'_{1n}e^{k_{sn}x}\right)\cos\left(k_{sn}y\right)\end{array}\right], \tag{17}$$

where $\overline{h} = g/\omega^2$. The first two terms describe the progressive waves that move in opposite directions, which result in standing waves. In addition, the bracket includes the linear, harmonic, and hyperbolic solutions. The solution also includes a series of waves in the vertical direction, which decay away from the wave paddles. In this solution, k_p, k_{sn} and $\overline{k}_{sn}$ are the wave numbers of the progressive and evanescent waves, respectively.

Imposing the no-flow conditions (7) and (8), the solution for the velocity potential function φ_2 becomes

$$\varphi_2 = A\cos h(k_p y)[\sin(k_p x - \omega t) + \sin(2k_p L - k_p x - \omega t)] + \cos(k_p b + \omega t)\left[\sum_{n=1}^{N} D_{2n}e^{-k_{sn}x}\cos(k_{sn}y)\right]. \tag{18}$$

It is seen that the progressive waves are the same as those in φ_1. However, some terms inside the brackets have been eliminated due to the imposition of the no-flow conditions. The general solution for the velocity potential function φ_3 without imposing any boundary condition will be

$$\varphi_3 = A\cos h\left(k_p y\right)\left[\sin\left(2k_p L - k_p x - \omega t\right) - \sin\left(2k_p b + k_p x + \omega t\right)\right]$$

$$+\cos(k_p b+\omega t)\begin{bmatrix}(B-cx-2bc)(\overline{h}-h+y)+e^{\frac{y}{\overline{h}}}\left(\overline{A}\cos\left(\frac{x+2b}{\overline{h}}\right)-\overline{B}\sin\left(\frac{x+2b}{\overline{h}}\right)\right)\\+\sum_{n=1}^{N}\left(\overline{D}_{1n}e^{\overline{k}_{sn}(x+2b)}+\overline{D}'_{1n}e^{-\overline{k}_{sn}(x+2b)}\right)\sin(\overline{k}_{sn}y)\\+\sum_{n=1}^{N}\left(D_{1n}e^{k_{sn}(x+2b)}+D'_{1n}e^{-k_{sn}(x+2b)}\right)\cos(k_{sn}y)\end{bmatrix}. \tag{19}$$

It can be seen that, contrary to potential functions φ_1 and φ_2, the progressive waves in φ_3 move in the same direction. In other words, in the fluid regions φ_3 and φ_4, the produced progressive waves and the waves reflected from the test model, move in the same direction. They superimposed to construct a resultant progressive wave. Similarly, imposing the no-flow condition of Eq. (13) and the radiation condition at $x \to -\infty$, one can obtain the velocity potential function φ_4 as

$$\varphi_4 = A\cos h(k_p y)[\sin(2k_p L - k_p x - \omega t) - \sin(2k_p b + k_p x + \omega t)] + \cos(k_p b+\omega t)\left[\sum_{n=1}^{N} D_{2n}e^{k_{sn}(x+2b)}\cos(k_{sn}y)\right], \tag{20}$$

where the progressive waves are the same as those in velocity potential function φ_3, which results in progressive waves in the fourth region. Now, substituting the potential function φ_2 into the free surface condition of Eq. (9) yields the following dispersion equations

$$\omega^2 = k_p g\tan h\left(k_p h\right), \tag{21}$$

$$\omega^2 = k_{sn} g\tan(k_{sn}h). \tag{22}$$

The first equation is the dispersion relationship for progressive waves, while the second one determines the wave numbers for evanescent waves that their amplitudes decrease exponentially away from the wave paddles. Considering Eq. (21) there is only one solution for k_p, while Eq. (22) gives rise to infinite number of solutions for k_{sn}. In the same way, substituting the potential function φ_1 into the free surface condition of Eq. (5) yields another dispersion equation as

$$\frac{g}{\omega^2 h}(\overline{k}_{sn}h) = \tan(\overline{k}_{sn}h). \tag{23}$$

It is notable that imposing the free surface conditions of Eqs. (10) and (12) leads to the same dispersion equation. To evaluate the unknown coefficients A, B, c, $\overline{A}$, $\overline{B}$, $\overline{D}_{1n}$, $\overline{D}'_{1n}$, D_{1n}, D'_{1n}, and D_{2n} the kinematic conditions on the wave paddles and the matching conditions at the common boundaries of the fluid regions should be utilized. Assuming harmonic and in-phase motion of the wave paddles and substituting the first potential function φ_1 into the kinematic condition on the wave paddle, i.e., Eq. (6) leads to the following equation

$$B + cx + \frac{\omega^2}{g}\left(\overline{A}\cos\left(\frac{\omega^2}{g}x\right) + \overline{B}\sin\left(\frac{\omega^2}{g}x\right)\right) + \sum_{n=1}^{N}\overline{k}_{sn}(\overline{D}_{1n}e^{-\overline{k}_{sn}x} + \overline{D}'_{1n}e^{\overline{k}_{sn}x}) = S_1(x)\omega. \tag{24}$$

Imposing the kinematic condition of Eq. (11) for the third region, is also leads to Eq. (24). In addition, substituting the associated velocity potentials into Eq. (15) gives

$$\begin{aligned}&Ak_p\cosh(k_p y) + c\left(\frac{g}{\omega^2} - h + y\right) + \frac{\omega^2}{g}e^{\left(\frac{\omega^2}{g}y\right)}\\&\quad\times\left(\overline{A}\cos\left(\frac{\omega^2}{g}b\right) + \overline{B}\sin\left(\frac{\omega^2}{g}b\right)\right)\\&\quad+\sum_{n=1}^{N}\overline{k}_{sn}\left(-\overline{D}_{1n}e^{\overline{k}_{sn}b} + \overline{D}'_{1n}e^{-\overline{k}_{sn}b}\right)\sin(\overline{k}_{sn}y)\\&\quad=\sum_{n=1}^{N}k_{sn}\left(D_{1n}e^{k_{sn}b} - D'_{1n}e^{-k_{sn}b}\right)\cos(k_{sn}y).\end{aligned} \tag{25}$$

Likewise, substituting the related velocity potentials into the first and second equations of (14) leads to the following relations, respectively

$$\begin{aligned}&c\left(\frac{g}{\omega^2} - h + y\right) + \overline{B}\frac{\omega^2}{g}e^{\left(\frac{\omega^2}{g}y\right)}\\&\quad+\sum_{n=1}^{N}\overline{k}_{sn}\left(-\overline{D}_{1n} + \overline{D}'_{1n}\right)\sin(\overline{k}_{sn}y)\\&\quad=\sum_{n=1}^{N}k_{sn}(D_{1n} - D'_{1n} - D_{2n})\cos(k_{sn}y),\end{aligned} \tag{26}$$

$$\begin{aligned}&B + \overline{A}\frac{\omega^2}{g}e^{\left(\frac{\omega^2}{g}y\right)} + \sum_{n=1}^{N}\overline{k}_{sn}\left(\overline{D}_{1n} + \overline{D}'_{1n}\right)\cos\left(\overline{k}_{sn}y\right)\\&\quad=\sum_{n=1}^{N}k_{sn}\left(D_{1n} + D'_{1n} - D_{2n}\right)\sin(k_{sn}y).\end{aligned} \tag{27}$$

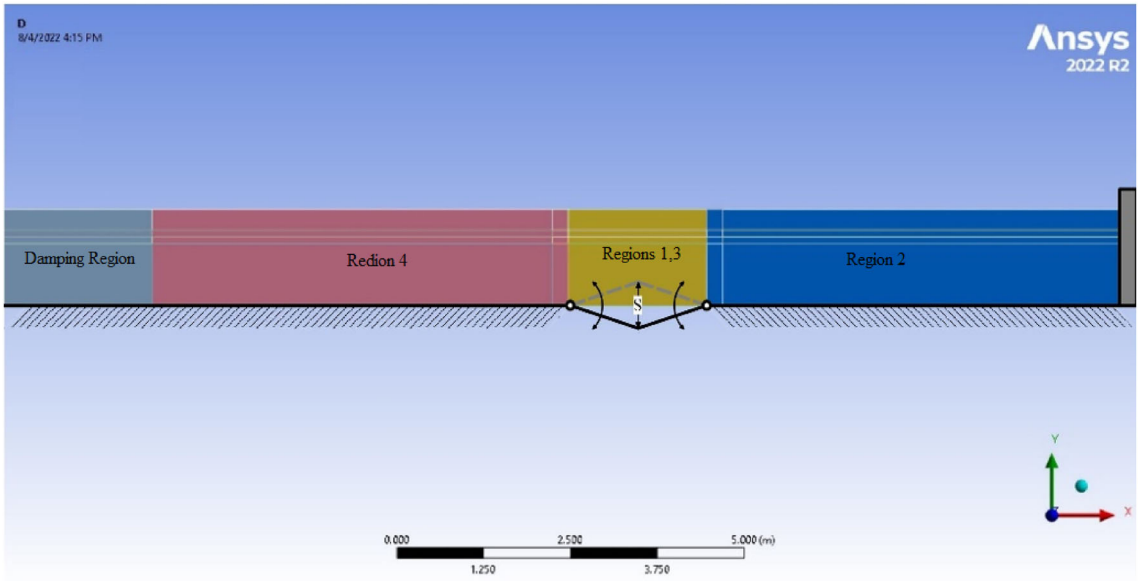

Fig. 2 The fluid domain utilized in ANSYS CFX simulation

It should be noted that the second relation of Eq. (15) and Eq. (16) are automatically satisfied and will not give independent equations. Now, employing the collocation method, Eqs. (24)–(27) are utilized to obtain the unknown coefficients. Application of the collocation method is explained in the results and discussion section. The main purpose of this paper is to create the desired wave elevations on the test structure, i.e., at the right end of the second fluid region φ_2 (at $x = L$). Hence, assuming atmospheric pressure at the free surface to be uniform (and chosen to be zero by convention) and neglecting the surface tension and nonlinear effects, the surface wave elevation on the test model becomes

$$\begin{aligned}\eta_{x=L} &= \frac{1}{g}\frac{\partial \varphi_2}{\partial t}\Big|_{\substack{y=h \\ x=L}} \\ &= \left(-\frac{\omega}{g}\right)\left\{2A\cos h\left(k_p h\right)\cos\left(k_p L-\omega t\right)\right. \\ &\quad \left.+\sin\left(k_p b+\omega t\right)\left[\sum_{n=1}^{N} D_{2n}e^{-k_{sn}L}\cos\left(k_{sn}h\right)\right]\right\}.\end{aligned} \tag{28}$$

The first term signifies the wave elevation of the standing waves, while the second term stands for the evanescent waves which decay rapidly away from the first fluid region. Therefore, the wave amplitude on the test structure at $x = L$ will be

$$H|_{x=L} = 2\left(\frac{\omega}{g}\right)A\cos h(k_p h). \tag{29}$$

3 Verification

The computational fluid dynamic software, ANSYS CFX is used to assess and verify the mathematical modeling presented in the previous section. In this verification, the infinite extent of the wave flume or radiation boundary condition is replaced by an absorbing or damping domain, as could be seen in Fig. 2. The finite volume method (Ansys 2021 R1) is used in the numerical simulation procedure to solve the governing continuity and Navier–Stokes's equations (Machado et al. (2018)). In addition, the volume of fluid method is utilized to determine the position of the free surface or air–water boundary (Liang et al. 2010). This numerical solution is in time domain.

In regions 2 and 4 ANSYS CFX 'Hexa' mesh is used to simulate the fluid field. In regions 1 and 3, ANSYS CFX dynamic mesh is used to simulate paddles interactions with the adjacent fluid. The dynamic mesh is set by activating the 'mesh deformation' option in ANSYS CFX PRE. This option allows the mesh to adapt to the wave paddles' motion by setting the boundary displacement equation through the ANSYS CFX CEL function (Maguire 2011).

To achieve better resolution in the numerical results, the mesh size near the free surface is reduced by using the edge sizing option (Havn 2011). In addition, to account for extreme changes in the magnitude and direction of the fluid velocity in regions 1 and 3, the mesh size used in these regions is about one-fifth of the mesh size in the regions 2 and 4.

Regarding the solution procedure of the numerical verification model, it was shown that the results of the nonlinear k-ε and SST models are not different from the results of the

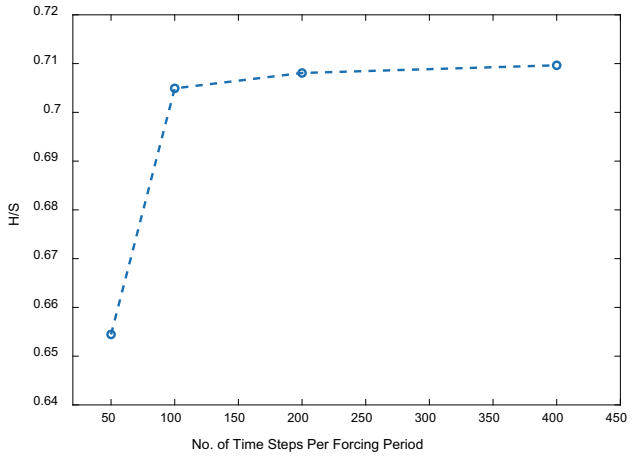

Fig. 3 Variations of the wave amplitude on the test model versus the time step ($S = 0.1$ m, $T = 1.5$ s)

laminar flow (Finnegan and Goggins 2012; Lal and Elangovan 2008). Hence, the laminar fluid flow is used in the analysis.

Considering the accuracy of the numerical solution, different time steps are suggested by different researchers. Recommendation for the optimal time step by Finnegan and Goggins (2012) and Ning and Teng (2007) are $T/50$ and $T/40$, respectively, where T denotes the wave period. At the same time, while suggested time step by Havn (2011) and Silva et al. (2010) is $T/100$, Machado et al. (2018) recommend $T/200$ as the optimal time step. In this study to determine the required time step, the impact of the adoption of different time steps on the resultant wave amplitude is investigated. Variations of the standing wave amplitude (wave height-to-stroke ratio *H/S*) measured on the test model versus the time step is depicted in Fig. 3. The monotonic convergence shows that the time step $T/200$ is sufficient to obtain an accurate numerical results. Therefore, this integration time step is adopted in all of the verification analyses.

4 Results and discussion

This section examines the performance of the proposed layout in producing surface waves. In addition, the effects of the reflected waves on the performance of the wavemaker are addressed. In the parametric study (Fig. 1), the assumed water depth is $h = 1$ m, the distance between the paddles and the test model is $L = 5$ m, and the length of each paddle is assumed to be $b = 1$ m.

The eigenfunctions corresponding to Eqs. (24)–(27) in both of the x and y directions are not mutually orthogonal sets. Consequently, instead of utilizing the Galerkin method, the collocation method is employed to determine the coefficients. To ensure accurate results, the collocation points employed in Eq. (24) must lie within the width of the first fluid zone ($-b \leq x \leq 0$). As for Eqs. (25), (26), and (27), the collocation points will be positioned along the y direction within the range of ($0 \leq y \leq h$). In deriving the simulation results, the number of collocation points will depend on the number of evanescent modes considered in the potential functions. In other words, increasing the number of modes, the number of unknown coefficients will increase and therefore more collocation points will be needed. On the other hand, contribution of higher modes can greatly influence the wave amplitude. Figure 4 shows the effect of the mode numbers of the evanescent components on the wave amplitude (wave height-to-stroke ratio *H/S*). It can be seen that as the number of modes increases, the rate of convergence grows, and contribution of eight modes is sufficient to reach results with good accuracy. Therefore, eight evanescent modes that results in 12 collocation points are utilized in the analysis.

The performance of the proposed layout, as evaluated by the analytical method, in producing surface waves is shown in Fig. 5. This figure shows the variations of the wave height-to-stroke ratio (*H/S*) with scaled wave number ($k_p h$) for different paddle length to water depth ratios (b/h). As could be seen, for different b/h values, wave amplitude reaches its maximum value at different wave numbers. In other words, in the range of waters with intermediate depth, a more significant share of the upward flow in fluid regions 1 and 3 is transmitted to the regions 2 and 4. For increasing paddle length, while the wave number corresponding to peak wave amplitude reduces, there is increase in the wave amplitude. This means higher performance of the system, but at the same time the effective operating range decreases.

To verify the analytical derivation, surface wave amplitude, in a particular case of '$b = h$', is compared with that evaluated by ANSYS CFX in Fig. 6, where the correlation of the analytical and numerical results seems acceptable.

Figure 7 shows the evolution of scaled wave amplitude with forcing period for different b/h ratios. This figure shows that transfer of fluid contents or energy between the fluid regions depends on the excitation period and the paddle length. As could be seen, for very small or large paddle length or for very low excitation periods, the produced wave elevation will be small and the gravity disturbs optimal energy transfer between fluid regions.

While in the region 2 the interference between the incident and reflected waves produces standing waves, in the region 4 the reflected waves and the incident waves propagate in the same direction, and their combination results in the creation of a new progressive waves. At the same time, in the fluid regions 1 and 3, a combination of standing and progressive waves is created. For comparison, the wave elevations during a forcing period (in this case $T = 1.5$ s) with time interval of $T/20$ as evaluated by the analytical derivation and ANSYS CFX are shown in Fig. 8. In the case of analytical solution, a

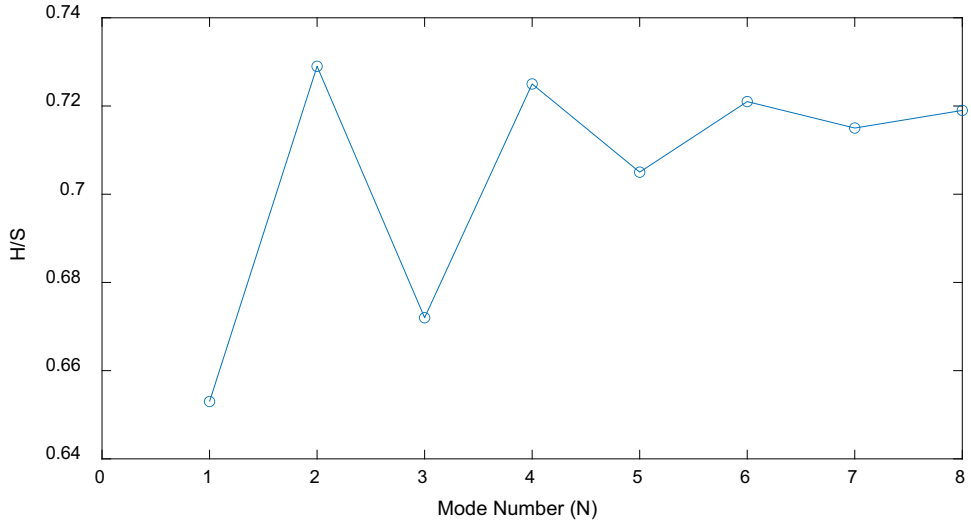

Fig. 4 Variations of the wave amplitude nearby the test model versus the mode number ($T = 1.5$ s)

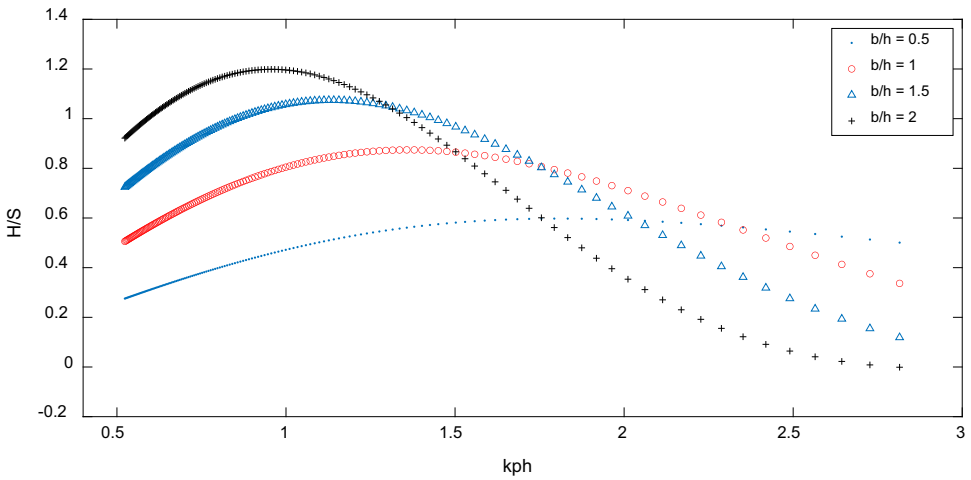

Fig. 5 Variations of the wave amplitude with scaled wave number for different values of the paddle lengths

minor mismatch can be seen in imposing compatibility conditions between the regions 1 and 2. This error is related to the number of collocation points used in boundary conditions of Eq. (14), and by increasing the number of collocation points, the accuracy of the solution could be improved. As could be seen, there is a good correlation between the analytical solution and ANSYS CFX results in the location of the nodes and anti-nodes and the amplitude of the standing waves. It is worth noting that the analytical solution is derived assuming steady state response in the frequency domain, where the numerical simulation using ANSYS CFX is based on transient analysis. Therefore, some discrepancy between the results is inevitable.

To have a closer insight on the trajectory of the water particles, especially on the common boundaries of the fluid regions that can help to assess the accuracy of the analytical solution, Fig. 9 depicts the path followed by fluid particles at various relative depths within the four distinct fluid regions. Notably, it can be observed that the trajectory of the particles within the second fluid region exhibits a reciprocal motion,

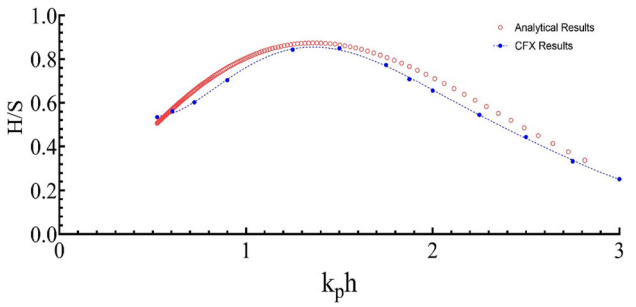

Fig. 6 Comparison of the wave amplitude adjacent the test model evaluated by the proposed formulation and ANSYS CFX

providing clear evidence of the presence of standing waves. Trajectories in the region 4 are elliptical near the free surface and decay exponentially with depth, which is the evidence of the progressive waves (Dean and Dalrymple 1991). As could be seen, in the regions 1 and 3, the trajectories show a smooth transition from standing to progressive waves.

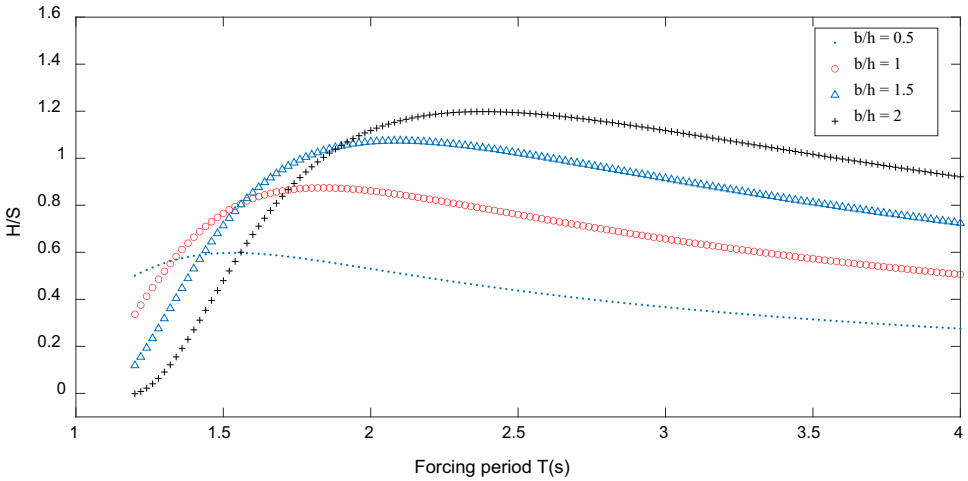

Fig. 7 Variations of the wave amplitude versus the forcing period for different paddle length

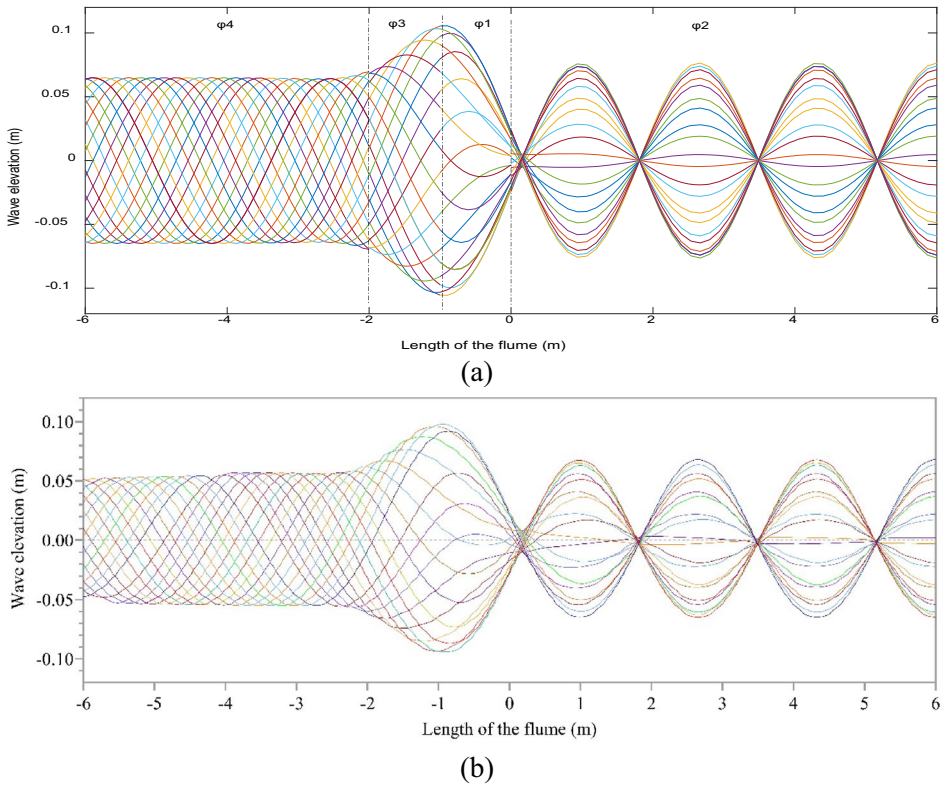

Fig. 8 Wave elevations in different time intervals ($T/20$) during a complete forcing period $T = 1.5$ s. **a** Analytical results, **b** ANSYS CFX results

Regarding the impact of the proposed layout on the performance of the flume, following conclusion could be obtained

- The proposed layout needs an absorbing boundary. While the presence of this absorbing boundary effectively eliminates the possibility of resonance in the system, it leads to longer flume length. In the following, it is discussed how by changing the layout, the flume length could be shortened.
- Re-reflection of progressive waves from wavemaker in the conventional flumes requires absorbing wavemakers. The proposed layout as will be discussed effectively diminishes this re-reflection.

These features are explored in Fig. 10, where evolution of wave elevation for different length of region 2 (different L) are evaluated. Considering the progressive waves in the region 4, the progressive wave generated by the wave paddles and the wave reflected from the test model, the amplitude or strength of the resultant progressive wave will depend on the phase difference between these waves. This means that by changing the position of the test model, the amplitude of the progressive wave in the fourth region can be controlled.

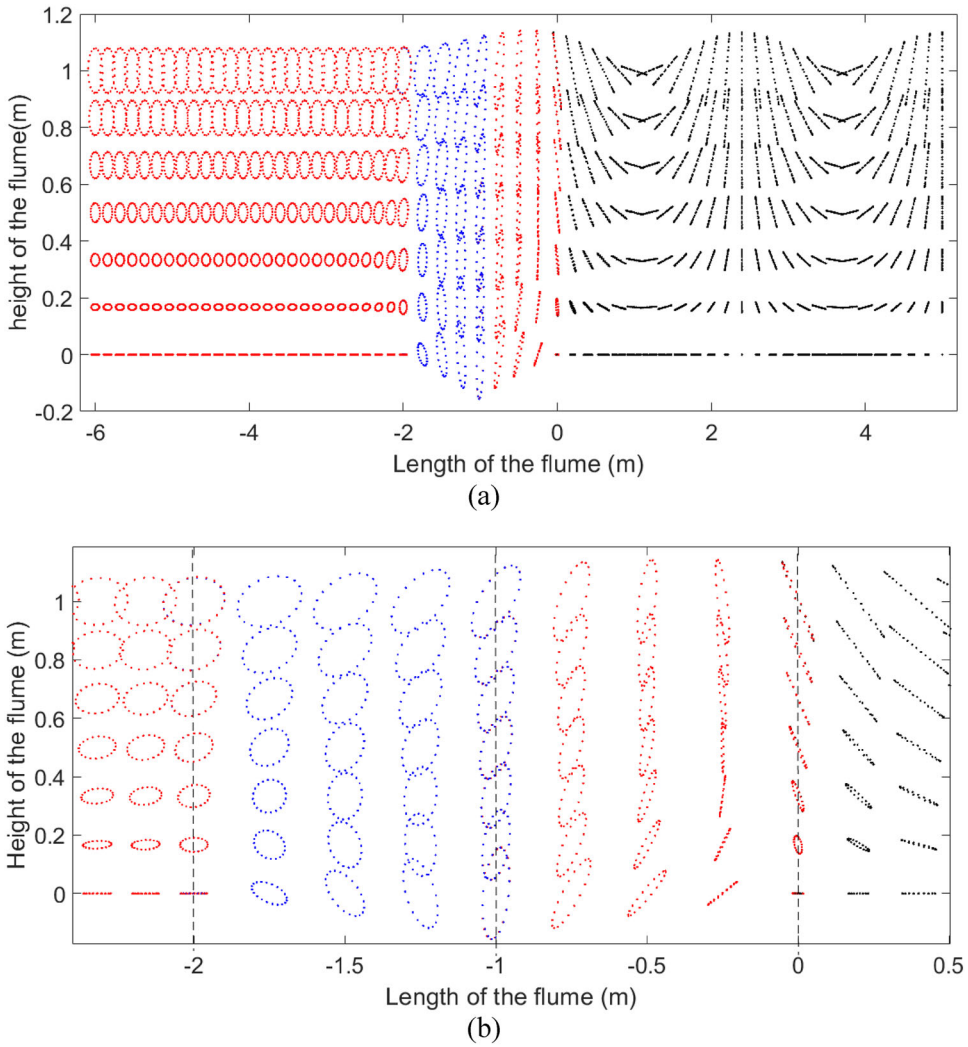

Fig. 9 **a** Fluid particle trajectories in the four fluid regions, **b** close up view of the fluid trajectories near the assumed boundaries of the fluid regions

For four different distance between the wavemaker and test model, variations of the amplitude of the resultant progressive waves are depicted in Fig. 10. It can be seen that for each wave length/period of excitation by tuning the flume layout, the wave amplitude in the region 4 can be diminished (Fig. 10d). In other words, the required energy absorption by the beach can be minimized and the maximum injected energy can be employed to create standing waves. This also provides the possibility of using smaller distance between the wavemaker and absorbing beach, which means the possibility of using flumes with shorter length.

Figure 10 shows that for all of the assumed L values, there is no progressive waves in the region 2. Figure 11 shows the effect of the test model position on the amplitude of standing waves in region 2 and progressive waves in region 4. As could be seen, while the amplitude of standing waves remains effectively the same, it could be possible to diminish the wave amplitude in the region 4. Invariance of the wave amplitude in the region 2, shows that the proposed layout could be used effectively to suppress the possibility of resonance in the system and at the same time, the proposed layout removes the need for absorbing wavemakers. It also demonstrates the possibility for decreasing the distance L, which means the shorter flume length. In this figure, the analytical results are also assessed with the numerical ANSYS CFX solutions. It should be pointed out that the numerical results are extracted assuming $\mathrm{d}t = T/100$.

5 Conclusion

Utilizing a hinge-type, bottom-mounted wavemaker, a new test layout was introduced for test of fully reflective models. The equations governing the fluid domain were analytically solved by dividing the fluid domain into four regions and using velocity potential functions for steady state excitation. Computational fluid dynamic software ANSYS CFX was

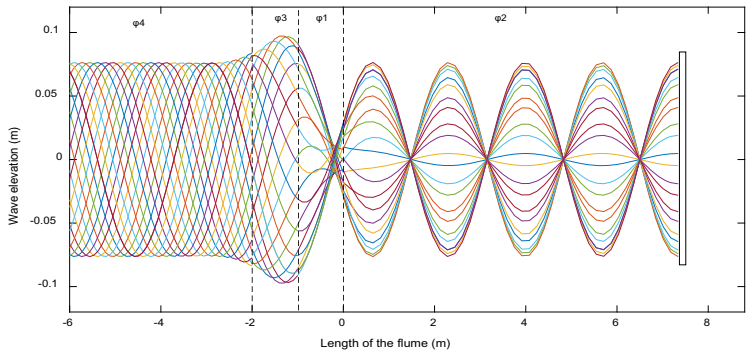

(a)

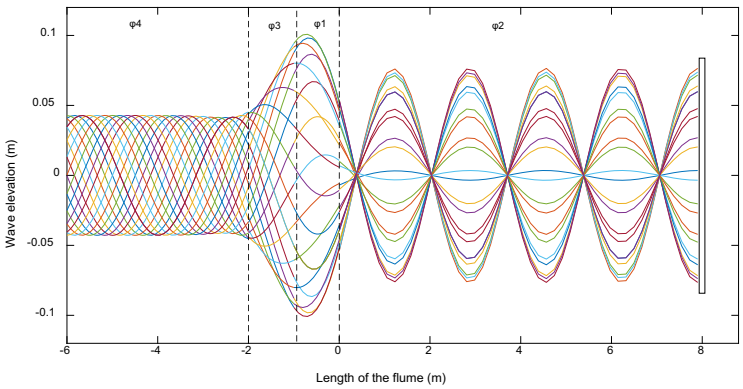

(b)

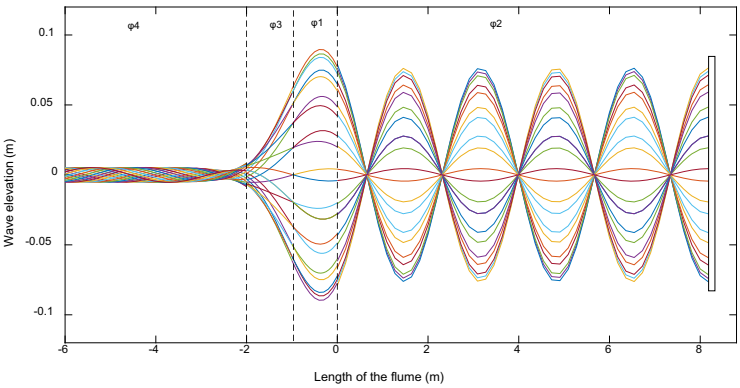

(c)

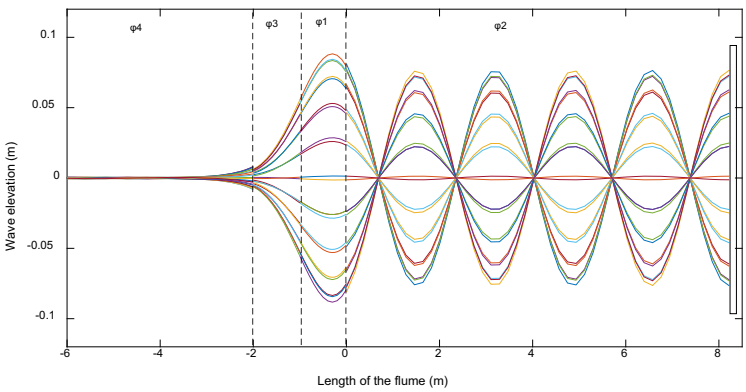

(d)

Fig. 10 The effect of geometry on the variation of the wave amplitude along the flume for different length of the region 2, **a** $L = 7.34$ m, **b** $L = 7.9$ m, **c** $L = 8.18$ m, **d** $L = 8.22$ m

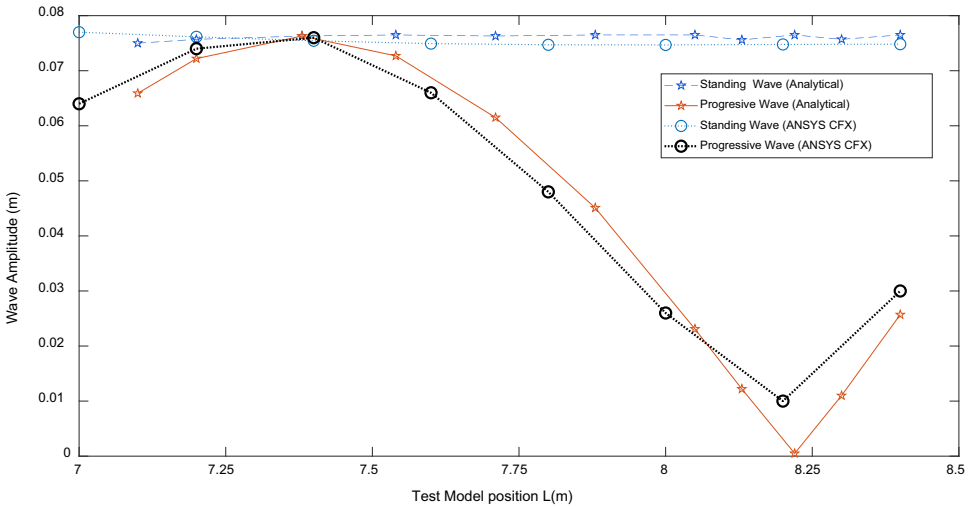

Fig. 11 Variation of the amplitude of progressive waves in region 4 and standing waves in region 2 as the test model is positioned differently

used to verify the analytical results. The proposed layout has the following characteristics:

- Use of bottom-mounted layout effectively eliminates re-reflection of progressive waves from the wavemaker. It is shown that the amplitude of standing wave between the wavemaker and test model is not affected by distance between the wavemaker and test model, which shows the possibility of reducing this distance without any adverse effect on the performance.
- Due to the use of absorbing beach, there is no possibility of resonance. It is also shown that by changing the distance between the wavemaker and test model, it is possible to diminish the amplitude of progressive waves develops between the wave maker and absorbing beach. This has two beneficial effects, a) there is no need for perfect absorbing beach, b) it could be employed to further reduce distance between the wavemaker and absorbing beach, which leads to shorter flume length.

Author contributions SM has done the mathematical modeling of the system RS prepared figures and the results and also wrote the manuscript text SP prepared the ANSYS results (Figs 2, 4, and 6b) ST reviewed the manuscript and cooperated in the discussions section.

Data availability The paper reports all the available data. However, the MATLAB m files used to generate the figures and data are not shareable due to their structure.

Declarations

Conflict of interest The authors declare no competing interests.

References

Bullock GN, Murton GJ (1989) Performance of a wedge-type absorbing wave maker. J Waterw Port Coast Ocean Eng 115(1):1–17

Christensen M, Frigaard P (1994) Design of absorbing wave maker based on digital filters. Hydraulics & Coastal Engineering Laboratory, Department of Civil Engineering, Aalborg University, Aalborg

Dean RG, Dalrymple RA (1991) Water wave mechanics for engineers and scientists. World Scientific Publishing Company, Singapore

Finnegan W, Goggins J (2012) Numerical simulation of linear water waves and wave–structure interaction. Ocean Eng 43:23–31. https://doi.org/10.1016/j.oceaneng.2012.01.002

Havn J (2011) Wave loads on underwater protection covers. Norges teknisk-naturvitenskapelige universitet, Fakultet for ingeniørvitenskap og teknologi, Institutt for marin teknikk, 2011. http://hdl.handle.net/11250/238072

Hirakuchi H, Kajima R, Kawaguchi T (1990) Application of a piston-type absorbing wavemaker to irregular wave experiments. Coast Eng Jpn 33(1):11–24. https://doi.org/10.1080/05785634.1990.11924520

Lal A, Elangovan M (2008) CFD simulation and validation of flap type wave-maker. World Acad Sci Eng Technol 46(1):76–82

Liang X-F, Yang J-M, Jun L, Xiao L-F, Xin L (2010) Numerical simulation of irregular wave-simulating irregular wave train. J Hydrodyn Ser B 22(4):537–545. https://doi.org/10.1016/S1001-6058(09)60086-X

Machado FMM, Lopes AMG, Ferreira AD (2018) Numerical simulation of regular waves: optimization of a numerical wave tank. Ocean Eng 170:89–99. https://doi.org/10.1016/j.oceaneng.2018.10.002

Maguire AE (2011) Hydrodynamics, control and numerical modelling of absorbing wavemakers. The University of Edinburgh, Edinburgh

Maguire A, Ingram D (2011) On geometric design considerations and control methodologies for absorbing wavemakers. Coast Eng 58(2):135–142. https://doi.org/10.1016/j.coastaleng.2010.09.002

Mahjouri S, Shabani R, Badiei P, Rezazadeh G (2020a) A bottom mounted wavemaker in water wave flumes. J Hydraulic Res. https://doi.org/10.1080/00221686.2020.1818314

Mahjouri S, Shabani R, Rezazadeh G, Badiei P (2020b) Active control of a piston-type absorbing wavemaker with fully reflective structure. China Ocean Eng 34(5):730–737. https://doi.org/10.1007/s13344-020-0066-9

Milgram JH (1970) Active water-wave absorbers. J Fluid Mech 42(4):845–859. https://doi.org/10.1017/S0022112070001635

Ning D, Teng B (2007) Numerical simulation of fully nonlinear irregular wave tank in three dimension. Int J Numer Meth Fluids 53(12):1847–1862. https://doi.org/10.1002/fld.1385

Schäffer HA, Klopman G (2000) Review of multidirectional active wave absorption methods. J Waterw Port Coast Ocean Eng 126(2):88–97

Schäffer HA, Jakobsen K (2003) Non-linear wave generation and active absorption in wave flumes. In: Proc. long waves symposium, Thessaloniki, Greece, pp 69–77. https://www.researchgate.net/publication/303247031

Silva M, Vitola MdA, Pinto W, Levi C (2010) Numerical simulation of monochromatic wave generated in laboratory: validation of a cfd code. In: 23th Congresso Nacional de Transporte Aquaviário, Construção Naval e Offshore, Rio de Janeiro, Brazil

Yang H-Q, Li M-G, Liu S-X, Zhang Q, Wang J (2015) A piston-type active absorbing wavemaker system with delay compensation. China Ocean Eng 29(6):917–924. https://doi.org/10.1007/s13344-015-0064-5

Yang H-Q, Li M-G, Liu S-X, Chen F-M (2016) An iterative re-weighted least-squares algorithm for the design of active absorbing wavemaker controller. J Hydrodyn Ser B 28(2):206–218. https://doi.org/10.1016/S1001-6058(16)60622-4

Zhou B-Z, Ning D-Z, Teng B, Liu S-X (2010) Analytical study on wave making in a deep wave flume in step-type. Wave Motion 47(1):1–11. https://doi.org/10.1016/j.wavemoti.2009.07.001